

**High-Resolution Global Land Surface Temperature Retrieval via a Coupled
Mechanism-Machine Learning Framework**

Tian Xie^a, Huanfeng Shen^{a,b,c,*}, Menghui Jiang^a, Juan-Carlos Jiménez-Muñoz^d, José A. Sobrino^d, Huifang Li^a, Chao Zeng^a

^a School of Resource and Environmental Sciences, Wuhan University, Wuhan 430079, China

^b Key Laboratory of Geographic Information System of Ministry of Education, Wuhan 430079, China

^c Key Laboratory of Digital Cartography and Land Information Application of the Ministry of Natural Resources, Wuhan 430079, China

^d Global Change Unit, Image Processing Laboratory, University of Valencia, Valencia 46980, Spain

^e State Key Laboratory of Information Engineering in Surveying, Mapping and Remote Sensing, Wuhan University, Wuhan 430079, China

***Corresponding author.**

E-mail address: shenhf@whu.edu.cn (H. Shen)

Abstract: Land surface temperature (LST) plays a crucial role in governing land-atmosphere interactions, surface energy balance, and climate processes. However, achieving high accuracy LST retrieval remains challenging under heterogeneous land cover and extreme atmospheric conditions. Traditional split window (SW) algorithms suffer from parameterization uncertainties that induce systematic biases in hot and humid environments; purely machine learning (ML) approaches, while capable of capturing complex nonlinearities, lack physical interpretability and generalization, leading to unstable performance when training data are scarce or out of distribution. To address these issues, we propose a coupled mechanism model-machine learning (MM-ML) framework that integrates physical constraints with data driven learning to achieve accurate and robust LST retrieval. The framework tightly fuses the radiative transfer (RT) process with data driven components through a multi stage modeling strategy, constructs training samples using MODerate resolution atmospheric TRANsmission (MODTRAN) simulations driven by global atmospheric profiles, and employs end-to-end physics-constrained optimization to enhance generalization. Validation against 4,450 ground observations from 29 globally distributed sites shows that MM-ML delivers the best performance across diverse ecosystems and climate zones, with a mean absolute error (MAE) of 1.84 K, root mean square error (RMSE) of 2.55 K, and coefficient of determination (R^2) of 0.966, markedly outperforming traditional SW, RT, and pure ML methods. Under extreme high temperature, high humidity, low temperature, and low water vapor conditions, MM-ML maintains stable performance, reducing errors by more than 50% relative to conventional approaches. Sensitivity analysis indicates that LST estimates are most sensitive to sensor radiance, followed by atmospheric water vapor, and are less dependent on surface emissivity; MM-ML exhibits lower sensitivity and higher stability under perturbations in all three inputs. These results demonstrate the effectiveness and advantages of the coupled modeling strategy for retrieving geophysical parameters. Overall, the MM-ML framework combines physical interpretability with nonlinear modeling capacity, providing a reliable pathway for high resolution LST retrieval in complex environments and offering new technical support for climate monitoring, hydrological modeling, and ecosystem studies.

Keywords: Land surface temperature; Thermal infrared remote sensing; splitting window; machine learning

1. Introduction

Land Surface Temperature (LST) is a key parameter governing land-atmosphere interactions, energy budgets, and climate processes (Li et al., 2013; Li et al., 2023). It plays a vital role in climate change monitoring (Li and Thompson 2021; Li et al., 2025), urban heat island effects (Shen et al., 2016), hydrological-cycle modeling (Anderson et al., 2012), and extreme heatwave forecasting (Gu et al., 2025). LST has been designated a priority measurement by the International Geosphere-Biosphere Program (IGBP) (Townshend et al., 1994) and incorporated into the NASA Earth System Data Record (ESDR) program (Hollmann et al., 2013). However, because Earth-system processes are complex, interactive, and inherently multi-scale (Shen and Zhang 2023), achieving high-resolution, high-accuracy LST retrieval over heterogeneous surfaces and under extreme atmospheric conditions remains a major challenge (Li et al., 2023).

Thermal infrared satellite remote sensing provides an irreplaceable means for continuous global LST monitoring (Duan et al., 2018; Li et al., 2013; Li et al., 2023). However, the thermal infrared radiative transfer process is strongly affected by atmospheric effects, making LST retrieval a prototypical ill-posed inverse problem (Li et al., 2013; Li et al., 2023). To address this, researchers have developed a variety of physically based inversion methods by approximating and simplifying the radiation transfer equation (Chen et al., 2015; Gillespie et al., 2011; Jimenez-Munoz et al., 2009; Jiménez-Muñoz et al., 2014; Jimenez-Munoz and Sobrino 2003, 2008; Qin et al., 2001; Rozenstein et al., 2014; Wang et al., 2016; Yu et al., 2014). Among these, the Slit Window (SW) algorithm exploits the differing atmospheric absorption in two adjacent thermal infrared bands to attenuate water-vapor effects (Jiménez-Muñoz et al., 2014; Jimenez-Munoz and Sobrino 2008) and has been widely adopted due to its compact form and favorable accuracy. Nevertheless, because SW relies on empirical parameterizations, it tends to accumulate systematic errors under extreme conditions such as high temperature and humidity (Duan et al., 2018; Li et al., 2013; Li et al., 2023; Yu et al., 2014), limiting its suitability for high-accuracy retrievals across globally complex scenarios.

In recent years, machine learning (ML) has shown strong potential for geophysical parameter retrieval (Bergen et al., 2019; Koldasbayeva et al., 2024; Reichstein et al., 2019; Yuan et al., 2020). By mining large datasets, ML can capture complex nonlinear relationships and markedly improve retrieval accuracy. Yet purely data-driven approaches often lack physical interpretability and cross-scenario generalization, and may yield physically inconsistent predictions when representative samples are scarce

or observations fall out of distribution (Shen and Zhang 2023). To mitigate these issues, “physics-first, then learning” cascaded designs have been explored to combine physical and learning models (Ma et al., 2024; Mao et al., 2018; Wang et al., 2021), but such schemes are typically shallow couplings that do not realize deep physical–data co-optimization. For SW in particular, a “knowledge-guided” fusion of SW and ML has been investigated (Cheng et al., 2025), demonstrating the feasibility of imposing physical constraints while learning mappings. However, most existing studies remain confined to moderate-resolution MODIS data and do not fully address scale effects, boundary transitions, or mixed-pixel issues at high resolution; moreover, many methods embed physics with a single neural network, offering limited energy-consistency constraints. Their generalization across continents and climate regimes, as well as robustness under extreme temperature–humidity conditions, also remains to be systematically validated.

To address the above issues, we propose a Mechanism Module-Machine Learning Coupled Framework (MM-ML). Within an end-to-end, physics-constrained neural network, four functional subnetworks are designed to characterize the nonlinear relationships associated with the key terms of the split-window (SW) formulation, enabling deep coupling and joint optimization under a global energy-consistency objective. Unlike single-network physics embedding, MM-ML grants each subnetwork greater degrees of freedom, thereby maximizing the role of physical constraints in feature learning and parameter estimation and maintaining robustness under complex atmospheres and heterogeneous surfaces.

Using Landsat 8 thermal-infrared observations as the core dataset, we systematically evaluate MM-ML across 29 sites spanning five continents. This assessment incorporates MODerate resolution atmospheric TRANsmission (MODTRAN)-driven simulation samples based on GAPRI and TIGR atmospheric profiles, reanalysis data, and global ground station observations, covering diverse land surfaces ranging from arid to humid, tropical to high-latitude, and urban to desert environments. In addition, extreme-scenario tests and parameter-sensitivity experiments were performed to quantify model stability and error sources under edge conditions and input uncertainties. The results show that MM-ML markedly outperforms conventional SW, radiative-transfer-based approaches, and pure ML baselines in both accuracy and robustness, while maintaining stable performance under extreme conditions, thereby validating the effectiveness and transferability of physically interpretable deep learning for high-resolution LST retrieval.

2. Datasets

2.1 Simulated Dataset

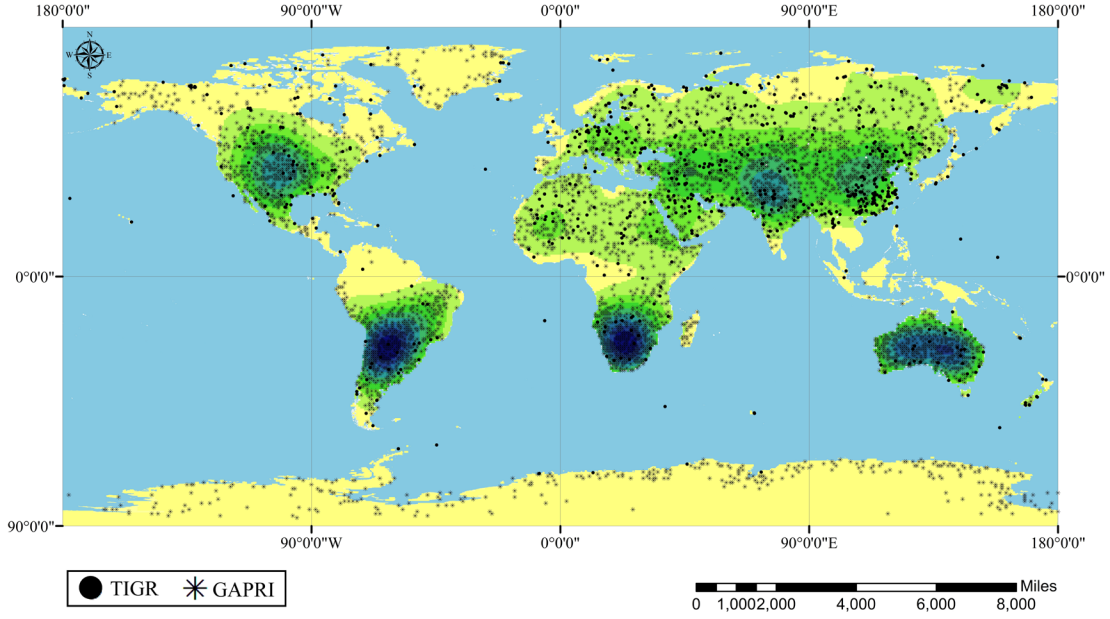


Fig. 1. Spatial distribution of atmospheric profile datasets. Coverage of the TIGR and GAPRI atmospheric profile datasets used in this study across global land areas.

This study first constructed a simulated dataset to ensure the generalizability of the method under varying atmospheric and surface conditions. The GAPRI atmospheric profile database, serving as a global collection of atmospheric vertical profiles, is widely utilized in LST inversion studies (Mattar et al., 2015). Covering a grid of approximately $0.75^\circ \times 0.75^\circ$ with a temporal resolution of 6 hours, the dataset comprises 29 vertical levels and 8,324 atmospheric profiles. It encompasses typical atmospheric types, including tropical, mid-latitude summer, mid-latitude winter, subarctic summer, subarctic winter, and different precipitation-eligible intervals (0–10 cm, 10–20 cm, 20–30 cm, 30–40 cm, 40–60 cm). The TIGR atmospheric profile database, derived from over 80,000 radiosonde reports, employs statistical sampling to yield 2,311 representative profiles (Chedin et al., 1985; Chevallier et al., 1998). These profiles document vertical distributions of temperature, water vapor, and ozone concentration, categorized into five air mass types: tropical, mid-latitude, subarctic, and others. To avoid interference from ocean pixels, this study exclusively selected atmospheric profiles over land areas, whose spatial distribution is shown in Fig. 1.

Based on these two profile types, this study employed the MODTRAN 5.2.2 (Berk et al., 2004). MODTRAN explicitly represents molecular absorption, water-vapor effects, and aerosol scattering,

while accounting for surface emission and reflection, solar/lunar illumination, and spherical refraction; it outputs TIR radiance and key atmospheric parameters, from which we assembled a comprehensive simulated dataset.

2.2 Ground-based validation dataset

The validation data originate from three international standard observation networks: the Baseline Surface Radiation Network (BSRN), the U.S. Surface Radiation Budget Network (SURFRAD), and the Heihe River Basin (HRB) integrated observation network in northwestern China. BSRN, established by the World Radiation Monitoring Center and operating since 1992, provides high-accuracy, sub-minute observations of shortwave and longwave radiative fluxes across the world's major climate zones, serving as a key benchmark for remote-sensing retrievals and radiative transfer models (Driemel et al., 2018). SURFRAD, operated by the U.S. National Oceanic and Atmospheric Administration (NOAA) since 1993, comprises seven sites spanning different U.S. climate regimes and supplies broadband solar and thermal infrared radiation along with photosynthetically active radiation, ultraviolet radiation, and meteorological variables; all data undergo rigorous quality control and are released daily (Augustine et al., 2000). HRB network, located in the arid region of northwestern China and covering cropland, Gobi, wetland, and alpine grassland surfaces, provides long-term in situ measurements supporting regional land-surface process studies (Yu et al., 2017; Yu et al., 2014; Yu et al., 2011).

For remote sensing inputs, we used the two thermal infrared bands of Landsat-8: B10 (center 10.9 μm ; 10.6–11.2 μm) and B11 (center 12.0 μm ; 11.5–12.5 μm), selecting imagery from 1 January 2013 to 31 December 2023. Surface emissivity was derived from the ASTER Global Emissivity Database (GED) v3 and estimated by combining spectral emissivity with a normalized difference vegetation index (NDVI) threshold approach to discriminate land-cover types. Atmospheric water vapor content was obtained from NCEP reanalysis at 6-hour resolution and linearly interpolated to match Landsat-8 overpass times.

We have divided the sites across the three networks into five regions by continent: Asia, Europe, North America, Africa, and South America. Detailed information for each site is provided in Table 1. Land surface temperature (LST) can be estimated using the following equation:

$$LST = \left[\frac{I_{\uparrow} - (1 - \varepsilon_b) \cdot I_{\downarrow}}{\varepsilon_b \cdot \sigma} \right]^{1/4} \quad (1)$$

Where I_{\uparrow} and I_{\downarrow} denote upwelling and downwelling thermal-infrared irradiance, σ is the Stefan–Boltzmann constant ($\sigma = 5.6705 \times 10^{-8} \text{ W} \cdot \text{m}^{-2} \cdot \text{K}^{-4}$), and ε_b is broadband emissivity converted from

spectral emissivity in the MODIS 8-day LST/Emissivity product (Wang et al., 2005) using the image acquired closest to each validation date.

Table 1

Summary of the global ground validation sites used in this study..

Area	Code	Name	Location	Num
Asia	AR	A'rou	38.0473N, 100.4643E	147
	CAP	Cape Baranova	79.27N, 101.75E	14
	DM	Daman	38.8555N, 100.3722E	168
	DSL	Dashalong	38.8399N, 98.9406E	117
	HH	Heihe	38.827N, 100.4756E	97
	HMZ	Desert	42.1135N, 100.9872E	269
	HZZ	Huazhaizi Desert steppe	38.7659N, 100.3201E	167
	JYL	Jingyangling	37.8384N, 101.116E	123
	SDQ	Sidaoqiao	42.0012N, 101.1374E	286
	TAT	Tateno	36.0581N, 140.1258E	104
	YK	Yakou	38.0142N, 100.2421E	45
	ZYSD	Zhangye wetland	38.9751N, 100.4464E	166
Europe	BUD	Budapest-Lorinc	47.4291N, 19.1822E	73
	CAB	Cabauw	51.968N, 4.928E	132
	NYA	Ny-Ålesund	78.9227N, 11.9273E	163
	PAY	Payerne	46.8123N, 6.9422E	291
	TOR	Toravere	58.2641N, 26.4613E	73
North America	BAR	Barrow	71.323N, 156.607W	41
	BND	Bondville	40.0519N, 88.3731W	205
	DRA	Desert Rock	36.6237N, 116.0195W	337
	FPK	Fort Peck	48.3078N, 105.1017W	308
	GWN	Goodwin Creek	34.2547N, 89.8729W	245
	PSU	Penn. State Univ	40.7201N, 77.9308W	68
	SEL	Selegua, Mexico Solarimetric	15.784N, 91.9902W	29
	SXF	Sioux Falls	43.7340N, 96.6233W	214
	TBL	Table Mountain, Boulder	40.1250N, 105.2368W	258
Africa	GOB	Gobabeb	23.5614S, 15.042E	216
	IZA	Izaña	28.3093N, 16.4993W	83
South America	OHY	Observatory of Huancayo	12.05S, 75.32W	11
SUM				4450

3. Methodology

3.1 Fundamentals of LST retrieval

According to Planck's law, any object with a temperature above absolute zero emits electromagnetic

radiation. Under local thermodynamic equilibrium, the spectral radiance of a blackbody at wavelength λ and temperature T is:

$$B_{\lambda}(T) = \frac{c_1}{\lambda^5 \left[\exp\left(\frac{c_2}{\lambda T}\right) - 1 \right]} \quad (2)$$

where $c_1 = 1.191 \times 10^8 \text{ W}\mu\text{m}^4\text{sr}^{-1}\text{m}^{-2}$ and $c_2 = 1.439 \times 10^4 \mu\text{m K}$ are radiation constants. Natural surfaces are not ideal blackbodies; their radiance must be corrected by the surface emissivity ε . In the idealized case, neglecting atmospheric effects, LST can be inferred directly from ε and $B_{\lambda}(T)$.

3.2 Radiative transfer equation

In real satellite observations, the measured radiance includes both surface emission and atmospheric emission. Under clear-sky conditions, the top-of-atmosphere (TOA) radiance received by the sensor can be expressed by the radiative transfer equation (RTE) as:

$$L_{sen} = \varepsilon B(T_s)\tau + (1 - \varepsilon)I \downarrow \tau + I \uparrow \quad (3)$$

where $B(T_s)$ is the blackbody radiance at surface temperature T_s . τ is the atmospheric transmittance, and $I \downarrow$ and $I \uparrow$ are the downwelling and upwelling atmospheric radiances, respectively. A representative application is the USGS Landsat Collection 2 Level-2 LST product, which builds on the RTE and integrates TOA brightness temperature and reflectance, the ASTER Global Emissivity Database (GED), ASTER NDVI, and reanalysis atmospheric profiles to generate standardized, high-spatial-resolution LST ([Cook et al., 2014](#)).

3.3 Split-window algorithm

To reduce dependence on real-time atmospheric parameters, the split-window (SW) approach exploits the different atmospheric absorption responses of two adjacent thermal-infrared window bands to suppress water-vapor interference and improve LST retrieval accuracy. Following the generic SW formulation of ([Jiménez-Muñoz et al., 2014](#)), LST is estimated as:

$$T_s = T_i + c_1(T_i - T_j) + c_2(T_i - T_j)^2 + c_0 + (c_3 + c_4\omega)(1 - \varepsilon) + (c_5 + c_6\omega)\Delta\varepsilon \quad (4)$$

Where T_i and T_j are the brightness temperatures in the two TIR bands, ε is the mean emissivity, $\Delta\varepsilon$ is the emissivity difference between the bands, ω denotes atmospheric water vapor content, and c_0 - c_6 are empirical coefficients obtained by regression on simulated datasets. While the SW algorithm provides a compact parameterization of the complex radiative transfer process, its empirical assumptions can lead to pronounced errors under hot and humid conditions.

3.4 Pure machine learning

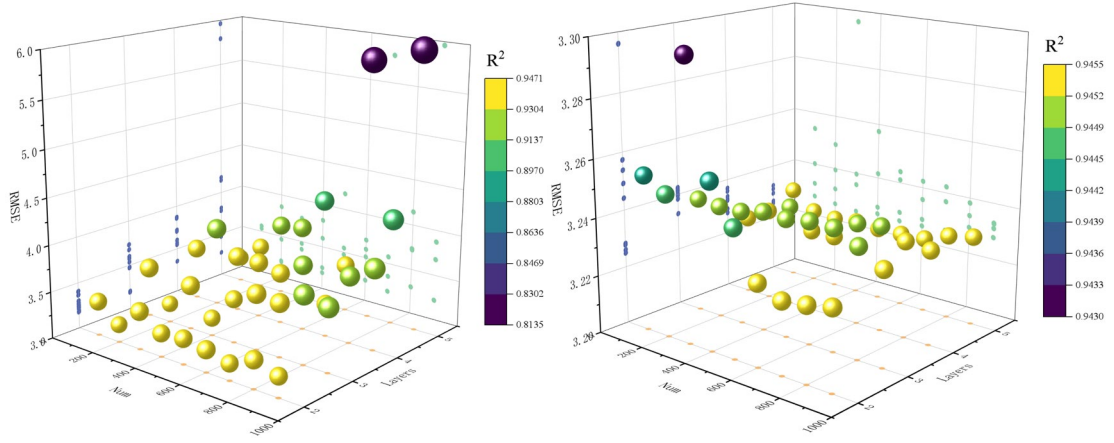


Fig. 2. Global site-based validation under different network configurations. Combinations of hidden-layer depth (2-5, step = 1) and neurons per layer (100-900, step = 100) are evaluated. Marker size encodes the mean absolute error (MAE), the Z-axis shows the root-mean-square error (RMSE), and color denotes the coefficient of determination (R^2). (a) ML.(b) MM-ML.

The pure machine learning (ML) baseline adopts a deep neural network (DNN), with the optimal architecture selected from the grid in Fig. 2 (a). Inputs comprise the sensor-received radiances L_{sen} in the two thermal-infrared bands, surface emissivity ε , and water vapor ω ; the output is LST. A sigmoid activation function is used to enhance nonlinear modeling capacity, and training is performed with the Adam optimizer (learning rate = 0.001) to mitigate vanishing gradients and improve convergence. Model generalization is evaluated via leave-one-site-out cross-validation (LOO-CV): in each fold, one site is withheld for testing while the remaining sites are used for training.

3.5 Mechanism model-machine learning coupled framework

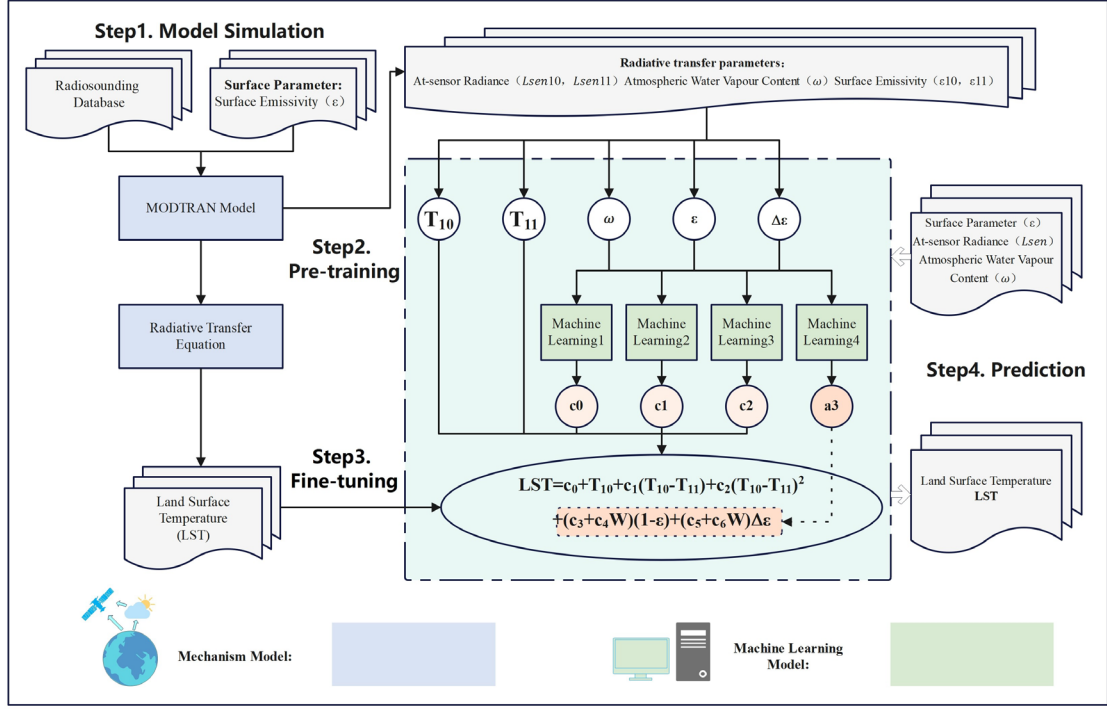


Fig. 3. Schematic diagram of the Mechanism Model-Machine Learning Coupling Framework (MM-ML). First, the MODTRAN model converts atmospheric profiles and surface state parameters into radiative transfer parameters, serving as inputs for the physically constrained neural network. During the pre-training phase, the learning process is embedded within the physical mechanism. In the fine-tuning phase, physical constraints are further deeply coupled with the learning process, achieving an organic integration of mechanism-based and data-driven methods. Ultimately, the trained MM-ML framework can accurately retrieve land surface temperature (LST) based on input parameters such as surface emissivity, entrance pupil radiance, and atmospheric water vapor content.

We proposed a coupled optimization framework integrating mechanisms, constraints, and machine learning based on the split-window algorithm (Fig. 3), aiming to combine the interpretability of MM with the nonlinear fitting capacity of ML for accurate and robust LST retrieval. The pipeline comprises four main stages: model simulation, pre-training, fine-tuning, and prediction.

During the sample-generation stage (Step 1), based on the GAPRI and TIGR atmospheric-profile databases, MODTRAN is used to simulate the radiative transfer process under different atmospheric conditions, producing a global, high-accuracy training dataset. MODTRAN accounts for molecular absorption, water-vapor absorption, and aerosol scattering, together with surface emissivity and the Landsat-8 TIR band spectral response functions—computes at-sensor brightness temperatures (T_{10}, T_{11}) from the satellite viewing geometry, as well as key radiative transfer parameters such as column water vapor (ω). In the pre-training stage (Step 2), we design four parallel ML subnetworks to regress the core functional parameters of the SW algorithm (c_0, c_1, c_2, a_3). The parameter a_3 corresponds to the physical

terms in the SW equation involving the brightness-temperature difference and its square, the mean surface emissivity, and the emissivity difference. Each subnetwork takes ε , $\Delta \varepsilon$, and ω as inputs and learns the nonlinear mappings from these variables to the model coefficients, enabling dynamic estimation of the function parameters. To enhance model generalization and physical consistency, in the fine-tuning stage (Step 3), the subnetwork-predicted parameters are substituted into the SW formula, and LST synthesized from the radiative transfer equation (RTE) is treated as the truth; a loss function targeting the prediction error is minimized via backpropagation to optimize the entire network end-to-end, thereby strengthening generalization and physical consistency. In the prediction stage (Step 4), the trained coupled model directly ingests observed brightness temperatures, emissivity, and water-vapor data to output high-accuracy LST retrievals. This fusion method markedly improves model performance and robustness under complex atmospheric conditions.

During model training, to mitigate overfitting risk, we systematically evaluated different network-configuration schemes (Fig. 2 (b)) and ultimately selected the best-performing design. All subnetworks adopt the sigmoid activation function, and weights are iteratively updated via the Adam optimizer, achieving coordinated mechanism-driven and data-driven modeling.

4. Result

4.1 Global site validation

4.1.1 Overall accuracy

To systematically evaluate the applicability and accuracy of different methods on a global scale, this study cross-validated four inversion schemes using 4,450 sets of surface temperature observations from 29 global sites. These schemes include the traditional split-window model (MM(SW)), the radiative transfer model (MM(RT)), a pure machine learning model (ML), and a coupled framework (MM-ML). The selected sites encompassed typical ecosystem types such as forests, grasslands, croplands, deserts, urban areas, and high-latitude snow-covered regions, effectively reflecting the performance of surface temperature inversion across diverse climatic zones and surface conditions.

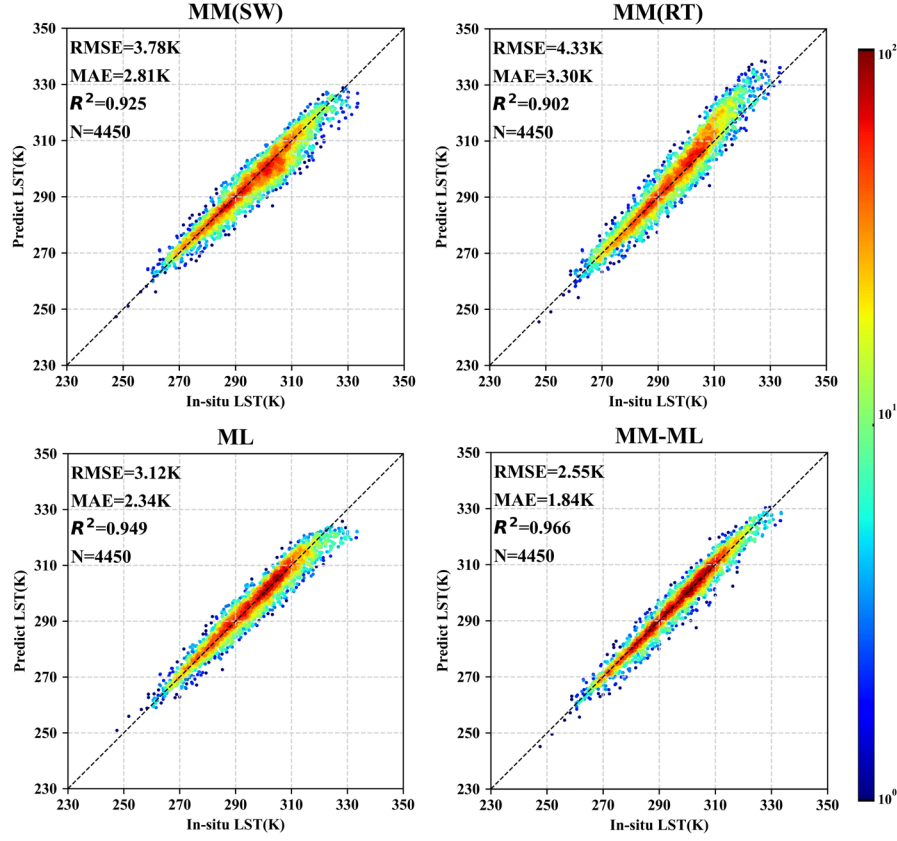
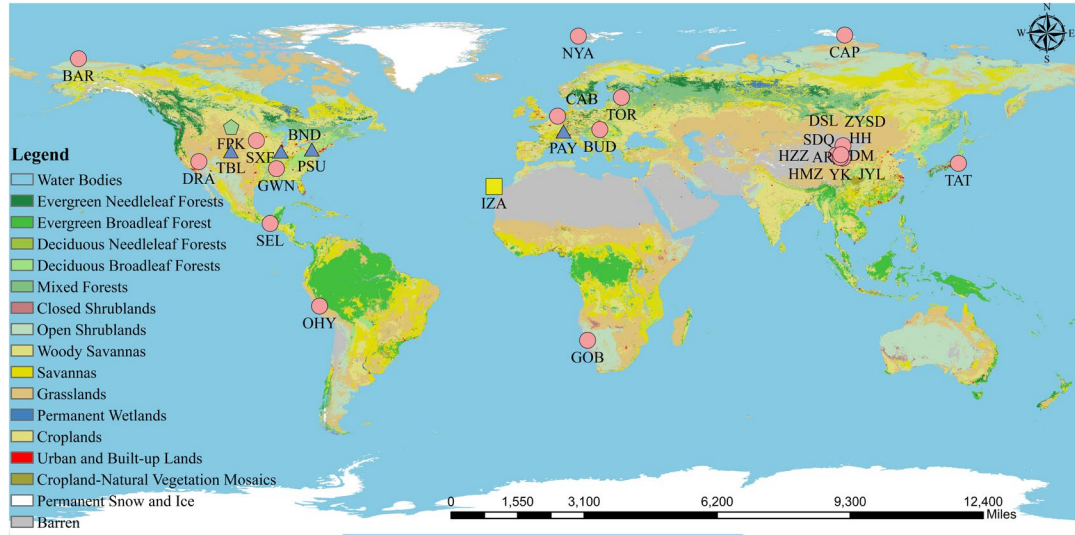


Fig. 4. Validation performance of four models across 29 global ground stations on five continents. (a) Mechanistic model based on the windowing method (MM(SW)). (b) Mechanistic model based on radiative transfer (MM(RT)). (c) Pure machine learning model (ML). (d) Mechanistic-machine learning coupled framework (MM-ML).

Global-scale validation results indicate that all four methods exhibit a degree of consistency in land surface temperature (LST) inversion, yet significant differences exist in accuracy and robustness (Fig. 4). Traditional mechanistic models MM(SW) and MM(RT) exhibited limited overall accuracy, with average RMSE values of 3.78 K and 4.33 K, respectively, and MAE values of 2.81 K and 3.30 K. Their errors increased significantly in regions with complex climatic conditions. The pure machine learning method ML significantly improved inversion accuracy, reducing the average RMSE to 3.12 K and MAE to 2.34 K, with a coefficient of determination R^2 of 0.949. However, substantial biases persist in regions with sparse high- or low-temperature samples. In contrast, the coupled MM-ML framework demonstrated optimal performance with an average RMSE of 2.55 K, MAE of 1.84 K, and R^2 improved to 0.966. This indicates the method's distinct advantage in integrating physical mechanisms with data learning capabilities.

4.1.2 Spatial distribution differences



	AR	DM	DSL	HH	HMZ	HZZ	JYL	SDQ	YK	ZYSD	BAR	BUD	CAB	CAP	GOB
MM(SW)	2.38	1.89	2.30	4.44	2.65	2.23	4.62	1.76	2.66	1.99	1.85	6.61	3.04	2.09	2.08
MM(RT)	2.55	2.51	2.40	3.99	5.83	4.43	5.96	2.07	2.75	1.56	2.03	3.14	1.95	2.55	5.72
ML	1.50	1.83	2.56	4.33	1.40	1.42	4.35	1.71	2.78	1.71	3.18	5.22	2.09	3.12	2.17
MM-ML	1.81	1.62	2.18	2.40	1.59	1.68	3.60	1.58	2.52	1.39	1.39	1.60	1.46	1.81	1.86
	IZA	NYA	OHY	PAY	SEL	TAT	TOR	BND	DRA	FPK	GWN	PSU	SXF	TBL	AVG
MM(SW)	2.69	2.23	6.96	3.80	3.96	6.60	4.98	2.74	2.76	1.92	3.38	2.77	1.47	2.96	2.81
MM(RT)	1.66	2.57	4.98	2.84	4.56	3.65	2.90	2.69	2.14	4.38	1.91	2.08	2.33	5.71	3.30
ML	2.96	2.54	4.76	1.47	1.76	5.22	2.30	1.52	4.19	2.65	1.73	1.38	1.47	2.05	2.34
MM-ML	1.68	1.79	2.00	1.83	1.92	2.56	1.57	1.88	1.92	2.01	1.41	1.55	1.43	2.31	1.84

Fig. 5. Accuracy assessment of four models across 29 ground observation stations on five continents. The 2020 global land use/land cover map was generated using the MCD12Q1 product ($0.05^\circ \times 0.05^\circ$ resolution), with validation station locations shown in the figure. The optimal model at each site is highlighted based on mean absolute error (MAE): the split-window mechanism model (MM(SW), green pentagons), the radiative transfer mechanism model (MM(RT), yellow squares), the pure machine learning model (ML, blue triangles), and the coupled mechanism-machine learning framework (MM-ML, red circles). Detailed site information is provided in Table 1. The lower panel displays the MAE values of the four models at each site, indicating that the MM-ML framework demonstrates superior and more stable performance.

The MAE statistics for each station further reveal spatial distribution differences among the various methods (Fig. 5). MM(SW) maintains relatively stable accuracy across most mid-to-high latitude regions, with an MAE of approximately 2 K in high-latitude areas (e.g., BAR, NYA, and CAP stations) and MAE exceeding 2 K in mid-latitude regions (e.g., FPK, SXF, DM, SDQ, and ZYSD stations) showed MAE values better than 2 K. However, errors significantly increased in high-temperature and high-humidity regions, such as tropical areas (e.g., OHY station, 6.96 K) and highly humid regions (e.g., TAT station, 6.60 K), indicating its limitations under such conditions. MM(RT) exhibits pronounced errors in hot, arid regions, such as GOB (MAE = 5.72 K) and OHY (MAE = 4.98 K), showing significant overestimation.

The ML method demonstrates lower overall error (MAE = 2.34 K) and performs well at most stations, though substantial bias persists in sparsely sampled extreme climate zones (e.g., OHY and TAT). Conversely, MM-ML achieved optimal or near-optimal performance across all 29 stations, with errors generally controlled between 1.4–2.5 K. For instance, in high-latitude cold regions (NYA, CAP) and typical arid zones (GOB, IZA), its MAE remained below 2 K, reducing errors by over 50% compared to MM(RT). It also exhibited the lowest deviations in mid-latitude urban and agricultural areas (e.g., TOR, BUD, CAB). These results demonstrate MM-ML's adaptability and stability across diverse climatic and surface conditions.

4.1.3 Regional Latitude Analysis

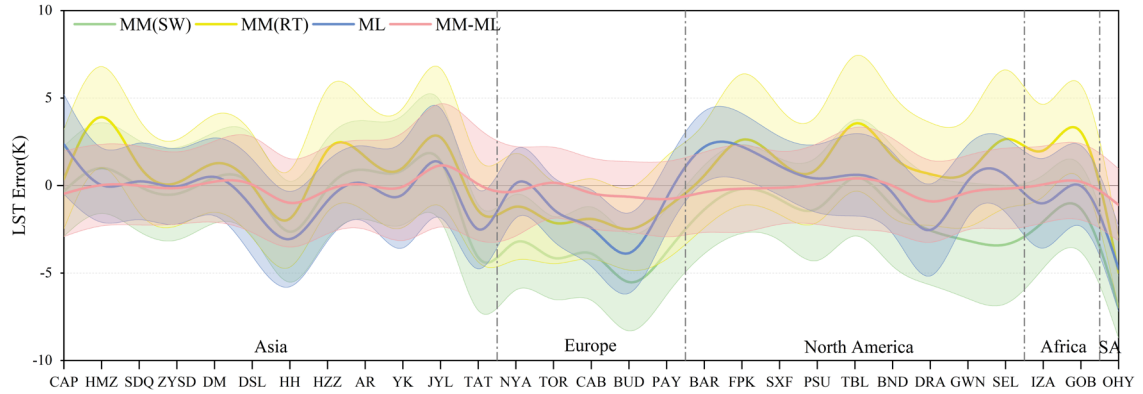


Fig. 6. Bias statistics of land surface temperature (LST) retrievals from four models (MM(SW), MM(RT), ML, and MM-ML) at global validation sites. Sites are grouped by continent (Asia, Europe, North America, Africa, and South America) and sorted by latitude from highest to lowest. Shaded areas indicate error distribution ranges, highlighting regional variations in retrieval performance under different climatic conditions.

From a latitudinal distribution perspective, the four methods exhibit significant performance differences across different climate zones, primarily influenced by atmospheric water vapor, temperature variations, and surface heterogeneity (Fig. 6).

In low-latitude tropical and subtropical regions (e.g., arid and semi-arid areas of Africa, highland regions of South America), atmospheric water vapor content is high, and surface temperature fluctuations are pronounced. MM(SW) exhibits substantial high-error bias with systematic deviations; MM(RT) generally overestimates values due to atmospheric profile uncertainties. The ML method mitigates systematic errors to some extent, but error distributions remain dispersed owing to insufficient extreme samples. MM-ML maintains low error and good stability in these regions through its integration of physical constraints and data-driven approaches.

In mid-latitude temperate zones (e.g., continental Europe and North American agricultural belts),

climatic conditions are relatively mild. However, due to high atmospheric humidity and complex land surface types in Europe, MM(SW) errors are significantly higher than in North America. ML performs well in well-sampled agricultural and urban areas but remains unstable during periods of intense temperature and humidity fluctuations. MM-ML demonstrates the most robust performance in this region, with biases consistently close to the zero-error line.

In high-latitude cold zones (e.g., Arctic and subarctic regions), where climates are dry and cold with predominantly ice-covered or frozen surfaces, MM(SW) and MM(RT) exhibit significantly increased errors due to limitations in low-temperature softness parameters and atmospheric profile accuracy. ML also shows substantial prediction fluctuations owing to sparse samples. Under these extreme conditions, MM-ML demonstrates optimal adaptability, with error fluctuations markedly lower than other methods.

In summary, MM(SW) exhibits substantial errors in high-temperature, high-humidity, and humid mid-latitude regions; MM(RT) generally overestimates temperatures; ML lacks stability in extreme temperature zones; while MM-ML maintains high accuracy and robustness across all latitudinal zones.

4.1.4 Typical Area Visualization Verification

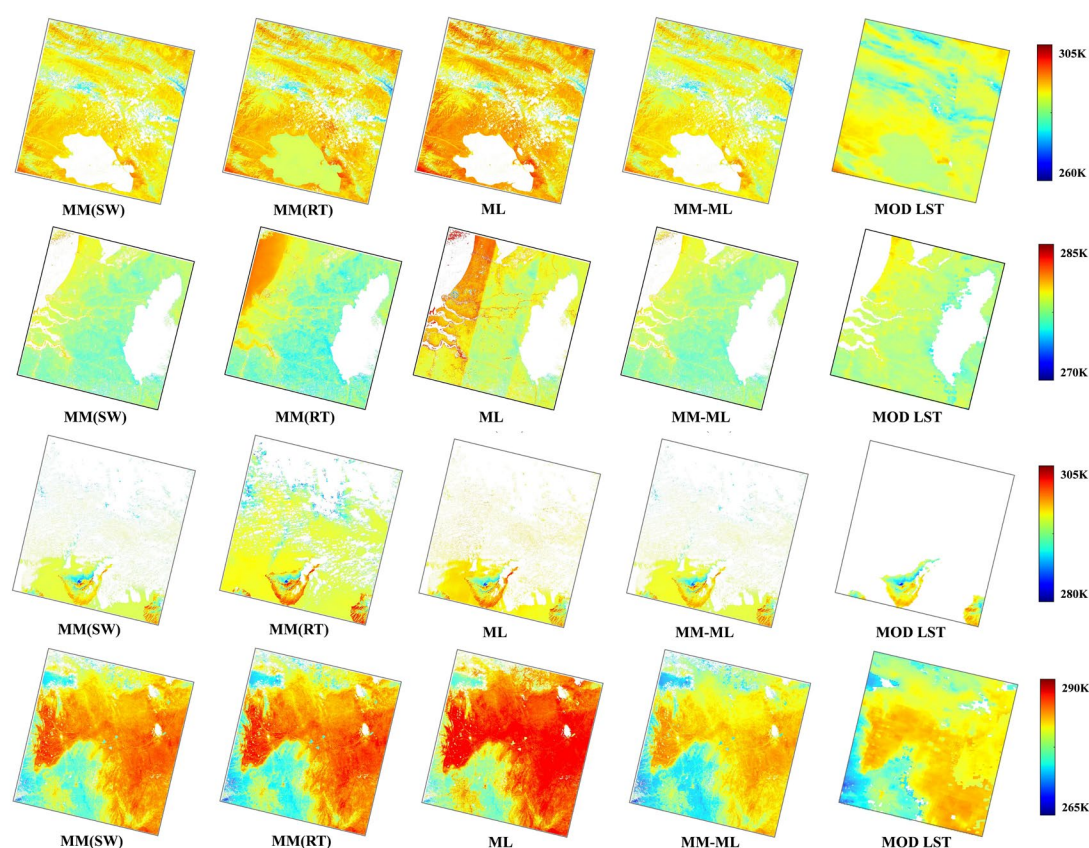


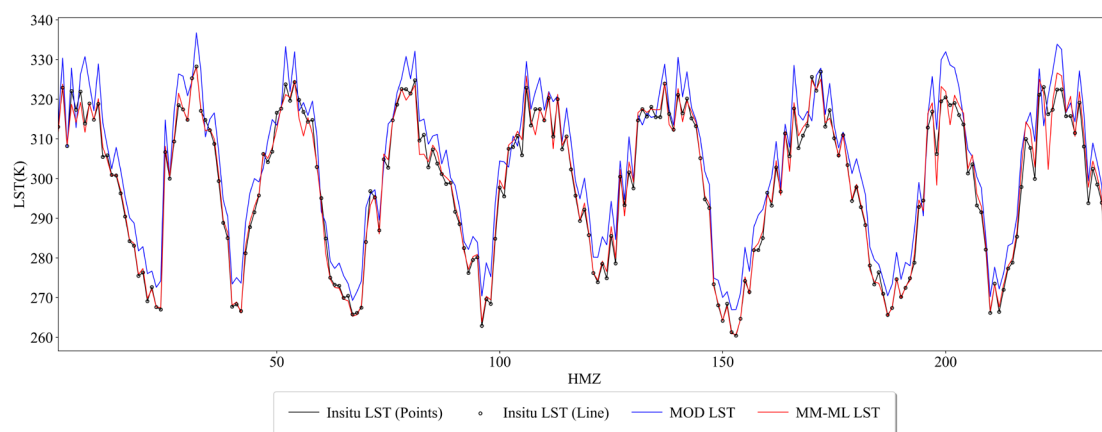
Fig. 7. Spatial comparison of LST retrieved by MM(SW), MM(RT), ML, and the proposed MM-ML with the MODIS LST product at representative sites on four continents. Sites include AR (Asia), CAB (Europe), IZA (Africa),

and TBL (North America). MM-ML shows the most consistent spatial patterns with MODIS LST, removing the large-scale biases observed in MM(SW) and MM(RT) and avoiding the local discontinuities seen in ML under complex land-atmosphere conditions.

To further visually compare the performance of different methods across representative regions, this study selected one representative site each from Asia (AR), Europe (CAB), Africa (IZA), and North America (TBL). The inversion results were compared with the currently most widely used MODIS LST product (Fig. 7).

At the Asian site, MM(RT) and ML exhibited significant overestimation, with particularly pronounced deviations in arid and low-vegetation areas. The MM-ML results showed the best spatial agreement with MODIS LST, with well-reconstructed temperature gradients and significantly reduced systematic bias. At the European site, ML produced unnatural boundaries in the inversion results due to abrupt changes in input parameters. Under physical constraints, MM-ML achieved smooth transitions, with its overall distribution highly consistent with the MODIS product. At sites in arid Africa, MM(RT) and ML showed significant overestimation in high-temperature zones; MM-ML effectively suppressed high-value biases, yielding temperature fields closer to reference products with higher reliability. At North American sites, MM(SW), MM(RT), and ML all exhibited pronounced overestimation. MM-ML demonstrated the highest spatial agreement with MOD LST products, maintaining stable accuracy across diverse regions.

4.1.5 Time Series Consistency Verification



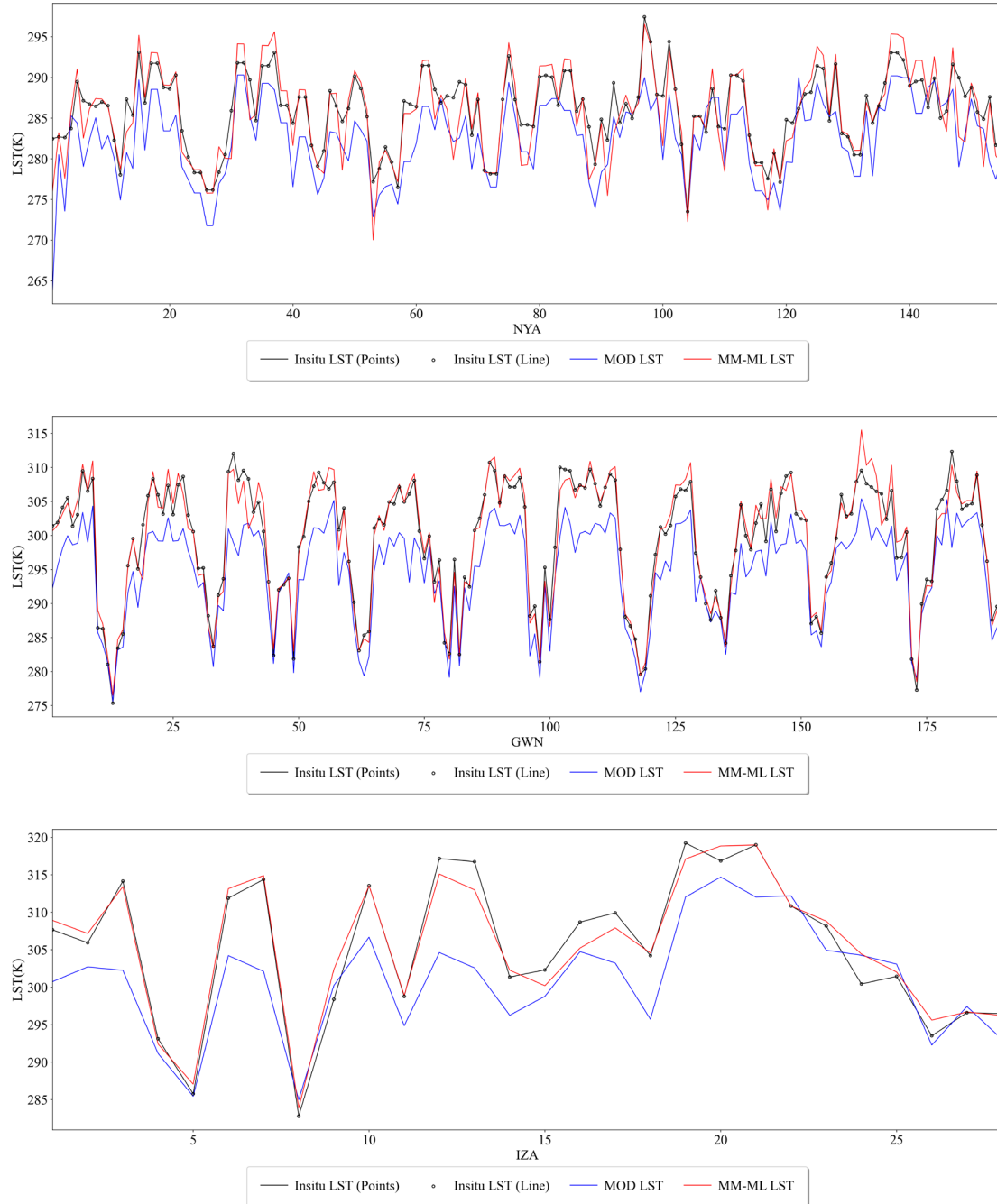


Fig. 8. Time-series comparison of MM-ML and MODIS surface temperatures with in-situ observations at four representative sites: HMZ in Asia, NYA in Europe, GWN in North America, and IZA in Africa.

To evaluate the temporal performance of MM-ML, this study selected representative sites across Asia (HMZ), Europe (NYA), North America (GWN), and Africa (IZA) for time-series comparisons between MM-ML retrieval results, MODIS products, and ground-truth measurements (Fig. 8).

The Asian HMZ site exhibited complex fluctuations typical of high-temperature, high-humidity conditions. The MOD LST product showed significant deviations, whereas MM-ML better fitted the observed sequence, particularly outperforming MOD LST during high-temperature phases. At the high-

latitude European NYA site, dominated by low temperatures and strong moisture influences, the MOD LST product exhibited large errors and intense fluctuations. In contrast, MM-ML stably tracked the observed sequence with significantly reduced errors. At the North American GWN site, MM-ML showed extremely high agreement with observed LST, accurately capturing diurnal variations and short-term fluctuations, while the MOD LST product exhibited a systematic underestimation overall. At the IZA site in Africa, located in an arid and hot region, the MOD LST product generally underestimates surface temperatures (with deviations exceeding 5 K). In contrast, MM-ML aligns closely with measured results at both temperature peaks and troughs, demonstrating strong adaptability to extreme conditions.

In hourly sequence comparisons across global representative sites, MM-ML consistently demonstrated optimal accuracy and stability. It not only overcame the systematic bias issues of MOD LST products under extreme climatic conditions but also exhibited high temporal consistency with observed results, further validating the reliability of the coupled framework for practical global-scale LST retrieval applications.

4.2 Extreme Conditions Validation

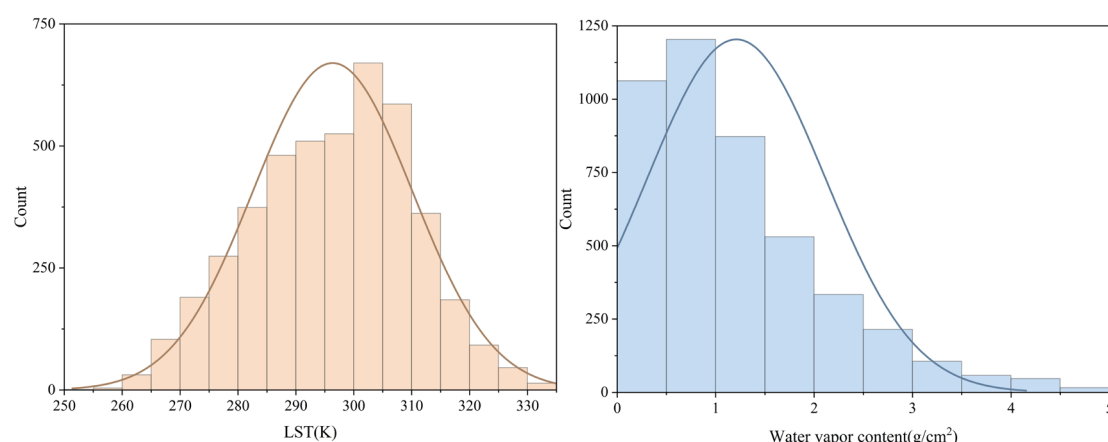


Fig. 9. Statistical distributions of (a) land surface temperature (LST) and (b) atmospheric water vapor in the global site-validation dataset. The histogram shows a dominance of moderate conditions (LST: approximately 280-310 K; water vapor: approximately 0.5-2.0 g/cm²), with fewer samples at the tails representing extreme cold/hot and dry/wet atmospheric states.

In the global validation dataset for Land Surface Temperature (LST) and atmospheric water vapor content distribution, the vast majority of samples cluster within conventional ranges (LST approximately 280-310 K, water vapor content approximately 0.5-2.0 g/cm²), while extreme samples at the distribution extremes are relatively scarce (Fig. 9). These marginal distributions not only represent extreme conditions of the surface and atmospheric environment but also constitute scenarios where model

accuracy and stability are most vulnerable to challenges. To systematically evaluate the adaptability of different methods under extreme conditions, this study defines the top 5% and bottom 5% of the entire dataset as representing extremely low/high temperatures and extremely low/high water vapor content, respectively, to characterize the most challenging marginal states.

4.2.1 Spatial Visualization Comparison

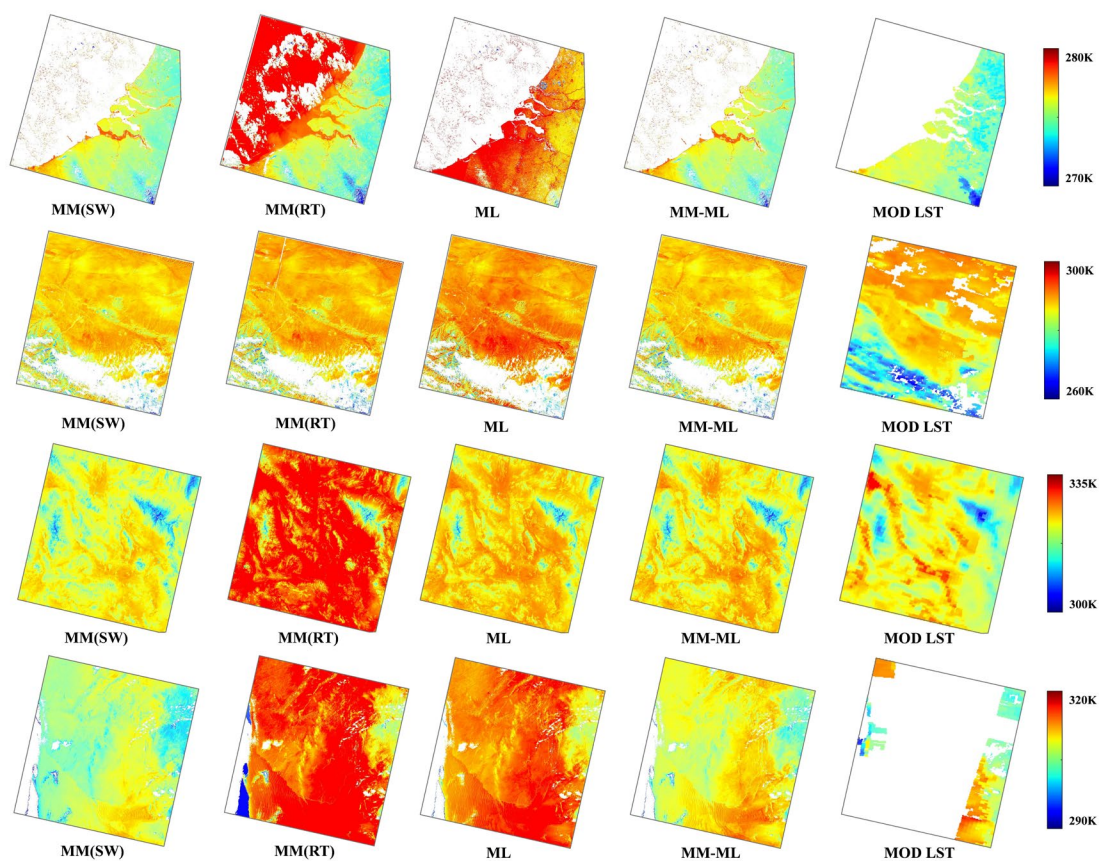


Fig. 10. Comparison of LST Inversion Results Under Four Extreme Scenarios. The spatial distributions of the following models were compared using MODIS Land Surface Temperature products: MM(SW), MM(RT), ML, and the proposed coupled framework (MM-ML). The four scenarios represent: (a) extremely low surface temperature at the European CAB site (274.64 K), (b) extremely low atmospheric water vapor content (0.08 g/cm²) at the Asian DM site, (c) extremely high surface temperature (328.55 K) at the North American DRA site, and (d) extremely high atmospheric water vapor content (3.59 g/cm²) at the African GOB site.

Under the extremely low temperature conditions at European CAB stations, as shown in Fig. 10(a), the ML shows a significant overall bias, exhibiting a pronounced overestimation that leads to a widespread overestimation of LST distribution. The results from MM(SW), MM(RT), and SW-ML are relatively close to the MOD LST product.

At the DM site in Asia under extremely low water vapor conditions, as shown in Fig. 10(b), both ML and MM(RT) exhibit significant overestimation, with ML showing more severe overestimation. The

overall distributions of MM(SW) and MM-ML methods align more closely with the MOD LST product. However, MM(SW) exhibits irregular deviations in locally complex terrain areas, while MM-ML results are smoother, demonstrating optimal spatial consistency and boundary transitions. This indicates that MM-ML can fully leverage mechanistic constraints to achieve high-precision inversion under low-humidity conditions.

Under extremely high-temperature conditions at the North American DRA site (Fig. 10c), both ML and MM(RT) methods overestimated temperatures, with MM(RT) exhibiting severe overestimation, leading to an overall elevated surface temperature field. The MM(SW) method captured the primary spatial patterns but showed significant underestimation in high-temperature zones. The MM-ML results aligned most closely with the MOD LST product, reproducing the overall high-temperature distribution while effectively suppressing systematic biases.

At the GOB site in Africa under extremely high moisture conditions (Fig. 10(d)), the mechanistic model exhibits systematic biases across large areas, with MM(RT) showing particularly severe deviations. While the ML method generally improves spatial distribution, it still exhibits noticeable distortions in regions with concentrated moisture anomalies. MM-ML effectively balances mechanistic constraints with data-driven advantages, exhibiting high spatial consistency with MOD LST products and demonstrating greater stability, especially in water vapor gradient zones.

4.2.2 Quantitative Results Analysis

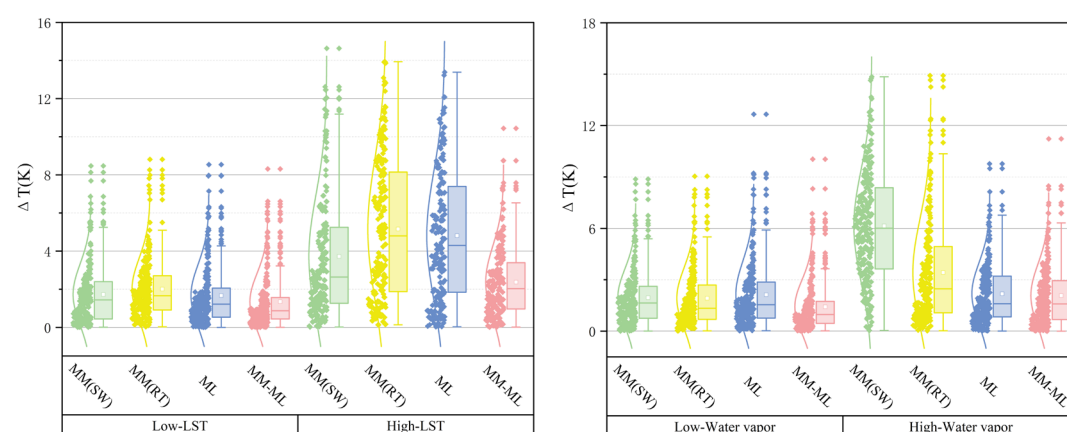


Fig. 11. Box-and-whisker plots of absolute surface temperature inversion errors under extreme atmospheric and surface conditions based on ground validation data. (a) Comparison between the lowest 5% and highest 5% atmospheric water vapor content (low-vapor and high-vapor conditions). (b) Comparison between the lowest 5% and highest 5% surface temperatures (low-surface-temperature and high-surface-temperature conditions).

Quantitative analysis results indicate (Fig. 11) that under extremely high-temperature conditions, the error of the mechanism model increases rapidly. The median of MM(RT) exceeds 4 K, with a maximum deviation reaching 14 K. ML shows slightly lower values, yet its median remains above 4 K. The MM(SW) method exhibits relative robustness, though its median error exceeds 2 K with extreme deviations exceeding 10 K. Under these conditions, MM-ML maintains its advantage with a median error of approximately 2 K and extreme deviations confined within 7 K. In conditions of extremely high water vapor, MM(SW) errors significantly amplify, with a median exceeding 6 K and extreme errors surpassing 14 K. MM(RT) showed slightly lower values, yet its extreme error still exceeded 10 K. ML and MM-ML exhibited relatively more robust performance. However, MM-ML's median bias hovered around 2 K and substantially reduced tail errors, outperforming ML to some extent.

Under extremely low-temperature conditions, MM(SW), MM(RT), and ML all exhibited systematic overestimation, with median errors exceeding 1 K and extreme errors surpassing 4 K. In contrast, MM-ML significantly reduces errors, controlling the median within 1 K and extreme errors below 4 K. Under extremely low humidity conditions, all methods show overall improvement, but single-mechanism models and ML exhibit median errors exceeding 1.5 K and extreme deviations still greater than 5 K. MM-ML performs optimally, with a median error below 1 K and extreme deviations remaining under 5 K.

Validation under extreme conditions further highlights differences between methods: traditional mechanistic models, constrained by parameterization assumptions, exhibit sharply amplified errors in high-temperature and high-humidity environments; pure machine learning approaches show pronounced fluctuations under high-temperature conditions with insufficient samples. In contrast, the coupled MM-ML framework demonstrated lower systematic bias and more stable error distributions across all four extreme scenarios, exhibiting remarkable robustness and adaptability. This provides a solid foundation for developing high-precision LST products tailored for complex environmental conditions.

4.3 Parameters Sensitivity Analysis

In surface temperature retrieval, input parameter uncertainties are the primary source affecting accuracy. Therefore, systematically evaluating the sensitivity of key parameters to retrieval results is essential. This study selected the thermal infrared band's entrance pupil radiance (B10, B11), surface emissivity (E10, E11), and atmospheric water vapor content (WATER) as the primary uncertainty factors.

Correlation analysis was first conducted, followed by sensitivity experiments based on these findings..

4.3.1 Correlation Analysis

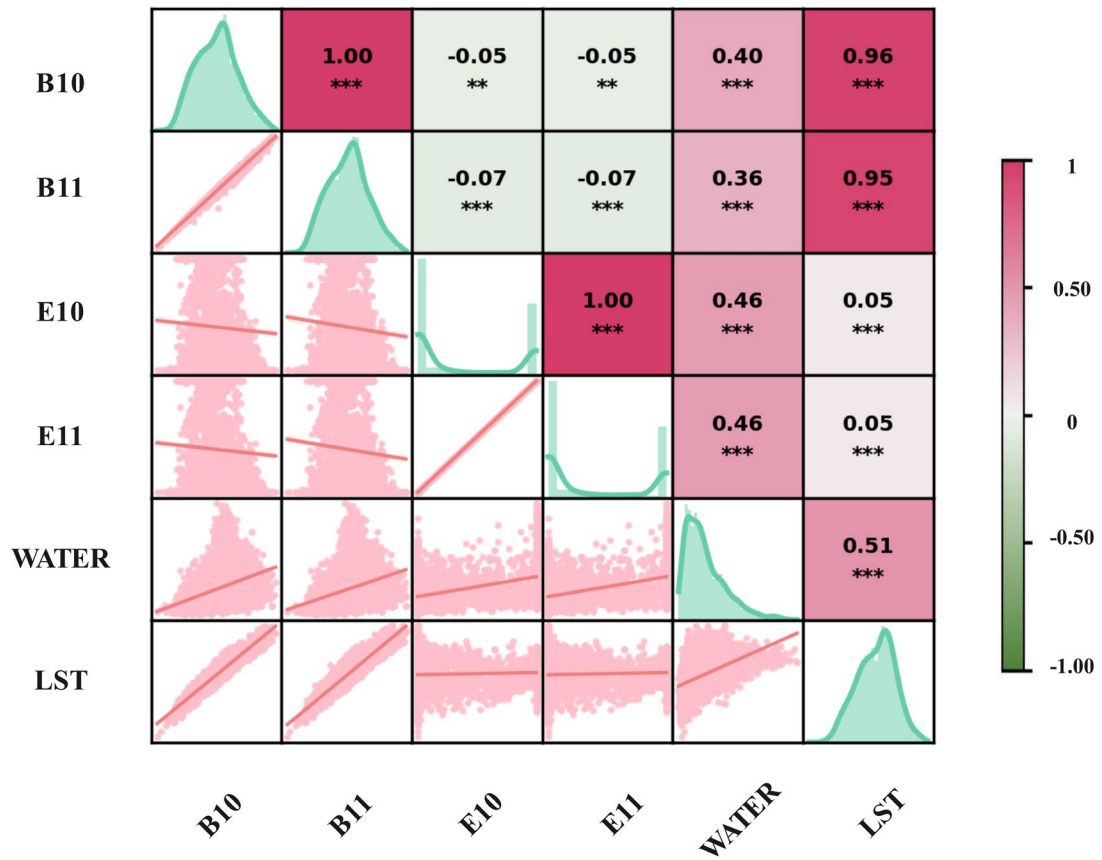


Fig. 12 Correlation analysis between input parameters (B10, B11, E10, E11, and water vapor content) and inverted land surface temperature (LST). Strong correlations were observed between sensor radiance (B10, B11) and LST, while emissivity (E10, E11) showed a weaker influence. Atmospheric water vapor content exhibited a moderate correlation.

Correlation analysis results indicate (Fig. 12) that LST exhibits a highly linear relationship with thermal infrared band entrance pupil radiance, with correlation coefficients of 0.96 and 0.95 for B10 and B11, respectively, confirming radiance as the core parameter driving LST retrieval. The correlation coefficient between atmospheric water vapor content and LST is 0.51, indicating a moderately strong positive correlation. This suggests that atmospheric water vapor plays a significant modulating role in LST retrieval during thermal infrared radiation transmission. In contrast, the correlation between surface emissivity and LST is only approximately 0.05, indicating a relatively weak overall influence. However, under specific surface conditions, it may still become a key source of uncertainty. This result provides a basis for subsequent sensitivity experiments.

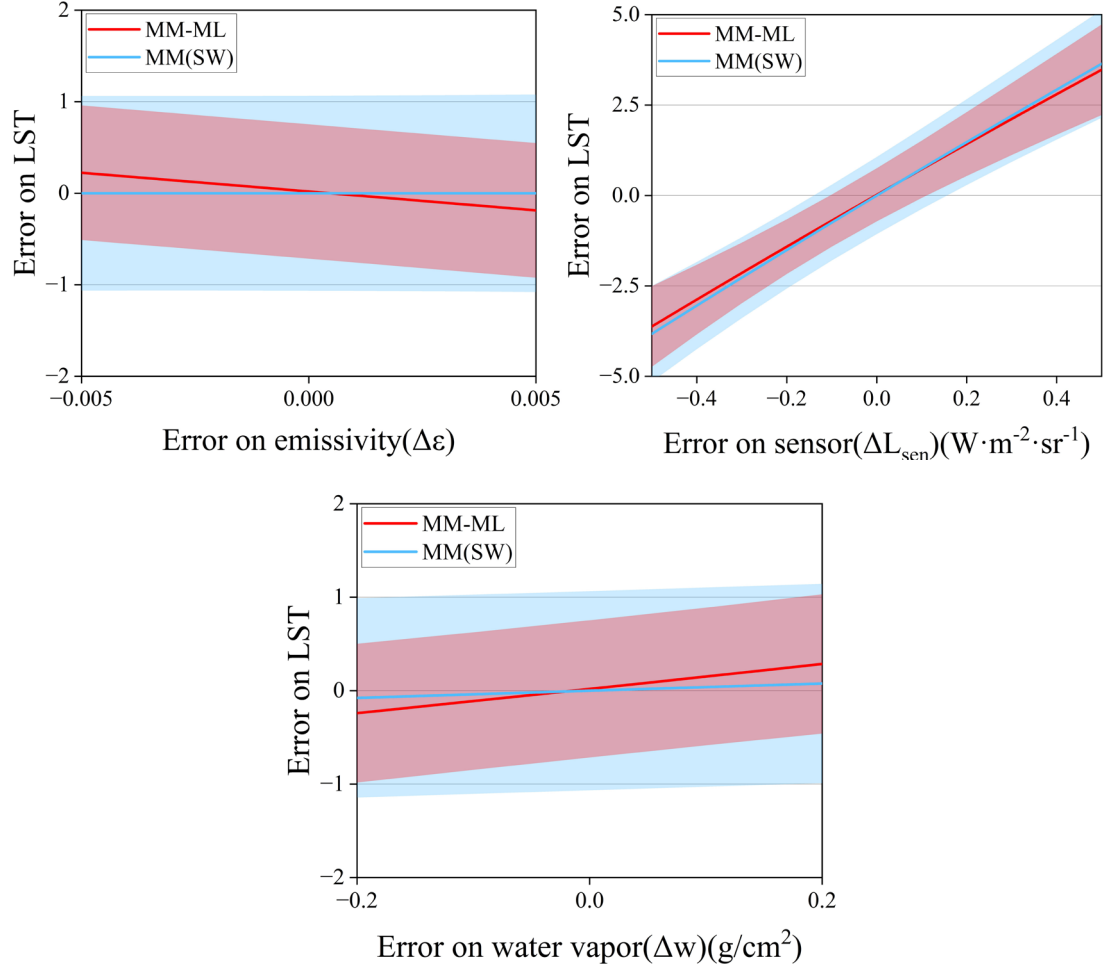


Fig. 13. Sensitivity analysis results of surface temperature (LST) retrieval accuracy to errors in surface albedo, satellite sensor entrance pupil radiance, and atmospheric water vapor content. The red curve and shaded area represent the mean error and confidence interval of the MM-ML model, while the blue curve and shaded area indicate the corresponding results for the MM(SW) model.

4.3.2 Sensitivity of Surface Emissivity

Statistical results (Fig. 13) indicate that under surface-specific emittance perturbations, the LST errors of MM(SW) and MM-ML exhibit minimal variation with emittance changes, with overall fluctuations confined within ± 1 K. Notably, MM-ML demonstrates only slight error variations with specific emittance deviations while maintaining consistently low error levels. This suggests that under most surface conditions, uncertainties in specific emittance exert limited influence on retrieval accuracy.

4.3.3 Sensitivity of in-sensor radiance

Under in-sensor radiance perturbations, LST errors exhibit the most pronounced variation. Both methods show linear dependence on sensor radiance deviations, with maximum errors exceeding ± 4 K, indicating that radiance accuracy is the primary source of uncertainty in LST retrieval. Comparatively,

the sensitivity curves of MM-ML and MM(SW) are nearly identical under this scenario. However, MM-ML exhibits superior stability within the error range, demonstrating its buffering effect even when radiance errors are present.

4.3.4 Atmospheric Water Vapor Sensitivity

Under atmospheric water vapor content perturbations, both MM(SW) and MM-ML exhibit LST errors that vary with water vapor deviations. However, the overall magnitude remains modest, with errors confined within ± 0.5 K. MM-ML demonstrates a more stable response to water vapor disturbances, exhibiting lower variability compared to MM(SW). This indicates MM-ML possesses greater adaptability to atmospheric condition uncertainties.

5. Discussion

5.1 Limitations of Traditional Methods

The findings of this study reaffirm the inadequacies of conventional surface temperature inversion methods. While mechanistic models provide reasonable estimates under typical conditions, their parameterization assumptions break down under high-temperature and high-humidity conditions, leading to significant amplification of systematic errors (Duan et al., 2018; Jiménez-Muñoz et al., 2014). Conversely, machine learning methods effectively capture complex nonlinear relationships in regions with sufficient training samples and balanced distributions, outperforming physical methods (Bergen et al., 2019; Reichstein et al., 2019). However, when training samples are insufficient or environmental conditions exceed the distribution range, ML often loses physical constraints, leading to unstable results or even deviations from physical laws (Shen and Zhang 2023). Therefore, single physical or single data-driven methods struggle to meet the high-precision inversion demands under globally diverse climates and surface environments.

5.2 Advantages of the Coupled Framework

The proposed MM-ML framework achieves complementary integration of mechanism modeling and data learning by deeply embedding physical constraints into the neural network architecture (Karniadakis et al., 2021; Reichstein et al., 2019; Willard et al., 2022). This strategy not only effectively overcomes the systematic biases of SW and RT methods under extreme conditions (Du et al., 2015; Li et al., 2013; Li et al., 2023; Wang et al., 2019) but also significantly enhances ML stability in marginal sample-scarce

regions(Cheng et al., 2025). Global multi-site validation demonstrates that MM-ML significantly outperforms traditional methods in both accuracy and robustness (reducing average RMSE by approximately 30% and lowering errors under extreme conditions by over 50%). The physical module provides interpretable boundary conditions(Bertels and Willems 2023; Xie et al., 2024), while the learning module enhances adaptability under complex atmospheric and surface conditions(Kim et al., 2024). This dual approach enables the model to exhibit stronger robustness and generalization capabilities across both routine and extreme environments(Bertels and Willems 2023).

5.3 Sources of Uncertainty and Model Adaptability

Parameter sensitivity analysis reveals distinct impacts of different input parameters on LST inversion errors. In-pupil radiance emerges as the primary uncertainty source, underscoring the critical importance of high-precision sensor calibration(Cheng et al., 2025). Atmospheric water vapor acts as the dominant modulating factor under humid conditions, where its uncertainty can significantly amplify inversion errors, particularly in tropical and monsoon climates(Dave et al., 2025; Islam et al., 2017; Jiménez-Muñoz et al., 2014; Jimenez-Munoz and Sobrino 2008). Surface emissivity has a relatively minor overall impact, but requires careful handling under bare soil and desert surfaces. Notably, MM-ML exhibits low sensitivity to perturbations in all three parameters, maintaining stability even under radiant brightness and water vapor input errors, indicating superior robustness and practical application potential.

5.4 Limitations and Future Prospects

Despite the strong performance of MM – ML across diverse environments, this study has several limitations. Notably, the current framework is unable to retrieve LST under cloudy conditions, which significantly restricts its operational applicability(Duan et al., 2018; Li et al., 2023). Future research may benefit from incorporating multi-source remote sensing techniques, such as fusing passive microwave and thermal infrared data, to enable all-weather LST retrieval(Zou et al., 2023); as well as leveraging high-resolution reanalysis datasets to improve temporal continuity and model robustness. The integration of lightweight deep neural networks and causal inference frameworks may further enhance the model's generalizability and explainability across heterogeneous environmental settings. Additionally, evaluating the model on various sensor platforms and temporal observation schemes is essential for expanding its applicability in global climate monitoring and early-warning systems for extreme weather events(Wang et al., 2025).

6. Conclusion

This study proposes a coupled modeling framework (MM-ML) integrating physical mechanisms with machine learning for high-precision surface temperature inversion, systematically validated across multiple global climate zones. Results demonstrate that MM-ML outperforms traditional mechanistic models and pure machine learning approaches in both accuracy and stability, adapting to diverse land surfaces and climatic conditions.

Under extreme conditions of high temperature, high humidity, low temperature, and aridity, MM-ML significantly reduces systematic errors of traditional methods and mitigates performance fluctuations of machine learning in sparsely sampled regions, demonstrating strong robustness and adaptability. Parameter sensitivity analysis indicates that in-pupil radiance is the primary source of uncertainty, followed by atmospheric water vapor, while surface emissivity has a relatively limited impact. MM-ML exhibits low sensitivity to multiple input errors, further demonstrating its robust interference resistance.

In summary, the MM-ML framework provides a reliable and efficient solution for LST retrieval under complex global environments. Future research can enhance the model's practicality and generalization by integrating multi-source remote sensing data, embedding stronger physical constraints, and extending it to multi-sensor platforms.

References:

- Anderson, M.C., Allen, R.G., Morse, A., & Kustas, W.P. (2012). Use of Landsat thermal imagery in monitoring evapotranspiration and managing water resources. *REMOTE SENSING OF ENVIRONMENT*, 122, 50-65
- Augustine, J.A., Deluisi, J.J., & Long, C.N. (2000). SURFRAD—A National Surface Radiation Budget Network for Atmospheric Research. *BULLETIN OF THE AMERICAN METEOROLOGICAL SOCIETY*, 81, 2341-2357
- Bergen, K.J., Johnson, P.A., De Hoop, M.V., & Beroza, G.C. (2019). Machine learning for data-driven discovery in solid Earth geoscience. *ence*, 363, eaau0323
- Berk, A., Anderson, G.P., Acharya, P.K., Bernstein, L.S., & Lewis, P.E. (2004). MODTRAN5: a reformulated atmospheric band model with auxiliary species and practical multiple scattering options. *Proceedings of SPIE - The International Society for Optical Engineering*, 5425, 341-347
- Bertels, D., & Willems, P. (2023). Physics-informed machine learning method for modelling transport of a conservative pollutant in surface water systems. *JOURNAL OF HYDROLOGY*, 619, 129354
- Chedin, A., Scott, N.A., Wahiche, C., & Moulinier, P. (1985). The Improved Initialization Inversion Method: A High Resolution Physical Method for Temperature Retrievals from Satellites of the TIROS-N Series. *Journal of Applied Meteorology*, 24, 128-143
- Chen, D., Huazhong, R., Qiming, Q., Jinjie, M., & Shaohua, Z. (2015). A Practical Split-Window Algorithm for Estimating Land Surface Temperature from Landsat 8 Data. *Remote Sensing*, 7, 647-665
- Cheng, Y., Wu, H., Li, Z., Götsche, F., Zhang, X., Li, X., Zhang, H., & Li, Y. (2025). A robust framework for accurate land surface temperature retrieval: Integrating split-window into knowledge-guided machine learning approach. *REMOTE SENSING OF ENVIRONMENT*, 318, 114609
- Chevallier, F., Chérut, F., Scott, N.A., & Chédin, A. (1998). A Neural Network Approach for a Fast and Accurate Computation of a Longwave Radiative Budget. *Journal of Applied Meteorology*, 37, 1385-1397
- Cook, M., Schott, J.R., Mandel, J., & Raqueno, N. (2014). Development of an Operational Calibration Methodology for the Landsat Thermal Data Archive and Initial Testing of the Atmospheric Compensation Component of a Land Surface Temperature (LST) Product from the Archive. In, *Remote Sensing* (pp. 11244-11266)
- Dave, J.A., Pandya, V., Goettsche, F., Varchand, H.K., Parmar, P.N., Desai, D.D., Kardani, D.B., Shah, D.B., Gujrati, A., Pathak, V.N., Trivedi, H.J., & Pandya, M.R. (2025). A hybrid physics-based method for estimating land surface temperature using radiative transfer simulations and machine learning model from Sentinel-3A SLSTR observations. *Earth Science Informatics*, 18, 150
- Driemel, A., Augustine, J., Behrens, K., Colle, S., Cox, C., Cuevas-Agull O, E., Denn, F.M., Duprat, T., Fukuda, M., Grobe, H., Haeffelin, M., Hodges, G., Hyett, N., Ijima, O., Kallis, A., Knap, W., Kustov, V., Long, C.N., Longenecker, D., Lupi, A., Maturilli, M., Mimouni, M., Ntsangwane, L., Ogihara, H., Olano, X., Olefs, M., Otori, M., Passamani, L., Pereira, E.B., Schmuth Usen, H., Schumacher, S., Sieger, R., Tamlyn, J., Vogt, R., Vuilleumier, L., Xia, X., Ohmura, A., & K Onig-Langlo, G. (2018). Baseline Surface Radiation Network (BSRN): structure and data description (1992--2017). *Earth System Science Data*, 10, 1491-1501
- Du, C., Ren, H., Qin, Q., Meng, J., & Zhao, S. (2015). A Practical Split-Window Algorithm for Estimating Land Surface Temperature from Landsat 8 Data. *Remote Sensing*, 7, 647-665
- Duan, S.B., Li, Z.L., Wang, C., Zhang, S., Tang, B.H., Leng, P., & Gao, M.F. (2018). Land-surface temperature retrieval from Landsat 8 single-channel thermal infrared data in combination with NCEP

reanalysis data and ASTER GED product. *INTERNATIONAL JOURNAL OF REMOTE SENSING*, 1-16

Gillespie, A.R., Abbott, E.A., Gilson, L., Hulley, G., Jiménez-Muñoz, J., & Sobrino, J.A. (2011). Residual errors in ASTER temperature and emissivity standard products AST08 and AST05. *REMOTE SENSING OF ENVIRONMENT*, 115, 3681-3694

Gu, L., Schumacher, D.L., Fischer, E.M., Slater, L.J., Yin, J., Sippel, S., Chen, J., Liu, P., & Knutti, R. (2025). Flash drought impacts on global ecosystems amplified by extreme heat. *Nature Geoscience*, 18, 709-715

Hollmann, R., Merchant, C.J., Saunders, R., Downy, C., & Wagner, W. (2013). THE ESA CLIMATE CHANGE INITIATIVE Satellite Data Records for Essential Climate Variables. *BULLETIN OF THE AMERICAN METEOROLOGICAL SOCIETY*, 94, 1541-1552

Islam, T., Hulley, G.C., Malakar, N.K., Radocinski, R.G., Guillevic, P.C., & Hook, S.J. (2017). A Physics-Based Algorithm for the Simultaneous Retrieval of Land Surface Temperature and Emissivity From VIIRS Thermal Infrared Data. *IEEE TRANSACTIONS ON GEOSCIENCE AND REMOTE SENSING*, 55, 563-576

Jimenez-Munoz, J.C., Cristobal, J., Sobrino, J.A., Soria, G., & Pons, X. (2009). Revision of the Single-Channel Algorithm for Land Surface Temperature Retrieval From Landsat Thermal-Infrared Data. *IEEE TRANSACTIONS ON GEOSCIENCE AND REMOTE SENSING*, 47, 339-349

Jiménez-Muñoz, J.C., Sobrino, J.A., Skoković, D., Mattar, C., & Cristóba, L.J. (2014). Land Surface Temperature Retrieval Methods From Landsat-8 Thermal Infrared Sensor Data. *IEEE Geoscience and Remote Sensing Letters*, 11, 1840-1843

Jimenez-Munoz, J.C., & Sobrino, J.A. (2003). A generalized single-channel method for retrieving land surface temperature from remote sensing data (vol 109, art no D08112, 2004). *Journal of Geophysical Research Atmospheres*, 108

Jimenez-Munoz, J.C., & Sobrino, J.A. (2008). Split-Window Coefficients for Land Surface Temperature Retrieval From Low-Resolution Thermal Infrared Sensors. *IEEE Geoscience and Remote Sensing Letters*, 5, 806-809

Karniadakis, G.E., Kevrekidis, I.G., Lu, L., Perdikaris, P., Wang, S., & Yang, L. (2021). Physics-informed machine learning. *Nature Reviews Physics*, 3, 422-440

Kim, I., Wook Kim, S., Kim, J., Huh, H., Jeong, I., Choi, T., Kim, J., & Lee, S. (2024). Single domain generalizable and physically interpretable bearing fault diagnosis for unseen working conditions. *EXPERT SYSTEMS WITH APPLICATIONS*, 241, 122455

Koldasbayeva, D., Tregubova, P., Gasanov, M., Zaytsev, A., Petrovskaya, A., & Burnaev, E. (2024). Challenges in data-driven geospatial modeling for environmental research and practice. *Nature Communications*, 15, 10700

Li, J., & Thompson, D.W.J. (2021). Widespread changes in surface temperature persistence under climate change. *NATURE*, 599, 425-430

Li, Y., Li, Z., Wu, H., Liu, X., Lian, X., Si, M., Li, J., Zhou, C., Tang, R., Duan, S., Zhao, W., Leng, P., Song, X., Shi, Q., Zhao, E., & Gao, C. (2025). Observed different impacts of potential tree restoration on local surface and air temperature. *Nature Communications*, 16, 2335

Li, Z., Tang, B., Wu, H., Ren, H., Yan, G., Wan, Z., Trigo, I.F., & Sobrino, J.A. (2013). Satellite-derived land surface temperature: Current status and perspectives. *REMOTE SENSING OF ENVIRONMENT*, 131, 14-37

Li, Z., Wu, H., Duan, S., Zhao, W., Ren, H., Liu, X., Leng, P., Tang, R., Ye, X., Zhu, J., Sun, Y., Si, M., Liu, M., Li, J., Zhang, X., Shang, G., Tang, B., Yan, G., & Zhou, C. (2023). Satellite Remote Sensing of

Global Land Surface Temperature: Definition, Methods, Products, and Applications. *REVIEWS OF GEOPHYSICS*, 61, e2022RG000777

Ma, J., Shen, H., Jiang, M., Lin, L., Meng, C., Zeng, C., Li, H., & Wu, P. (2024). A mechanism-guided machine learning method for mapping gapless land surface temperature. *REMOTE SENSING OF ENVIRONMENT*, 303, 114001

Mao, K., Zuo, Z., Shen, X., Xu, T., Gao, C., & Liu, G. (2018). Retrieval of Land-surface Temperature from AMSR2 Data Using a Deep Dynamic Learning Neural Network. *Chinese Geographical Science*, 28, 1-11

Mattar, C., Duran-Alarcon, C., Jimenez-Munoz, J.C., Santamaria-Artigas, A., Olivera-Guerra, L., & Sobrino, J.A. (2015). Global Atmospheric Profiles from Reanalysis Information (GAPRI): a new database for earth surface temperature retrieval. *INTERNATIONAL JOURNAL OF REMOTE SENSING*, 36, 5045-5060

Qin, Z., Karnieli, A., & Berliner, P. (2001). A mono-window algorithm for retrieving land surface temperature from Landsat TM data and its application to the Israel-Egypt border region. *INTERNATIONAL JOURNAL OF REMOTE SENSING*, 22, 3719-3746

Reichstein, M., Camps-Valls, G., Stevens, B., Jung, M., Denzler, J., Carvalhais, N., & Prabhat (2019). Deep learning and process understanding for data-driven Earth system science. *NATURE*, 566, 195-204

Rozenstein, O., Qin, Z., Derimian, Y., & Karnieli, A. (2014). Derivation of Land Surface Temperature for Landsat-8 TIRS Using a Split Window Algorithm. *SENSORS*, 14, 5768-5780

Shen, H., Huang, L., Zhang, L., Wu, P., & Zeng, C. (2016). Long-term and fine-scale satellite monitoring of the urban heat island effect by the fusion of multi-temporal and multi-sensor remote sensed data: A 26-year case study of the city of Wuhan in China. *REMOTE SENSING OF ENVIRONMENT*, 172, 109-125

Shen, H., & Zhang, L. (2023). Mechanism-learning coupling paradigms for parameter inversion and simulation in earth surface systems. *Science China Earth Sciences*, 66, 568-582

Townshend, J.R.G., Justice, C.O., Skole, D., Malingreau, J.P., & Ruttenberg, S. (1994). The 1 km resolution global data set: needs of the International Geosphere Biosphere Programme. *INTERNATIONAL JOURNAL OF REMOTE SENSING*, 15, 3417-3441

Wang, B., Zhou, F., Leng, P., Bai, Y., Zhang, X., & Shang, G. (2025). Land Surface Temperature Retrieval From Channel Resolution Enhanced FY-3D/MWRI Observations. *IEEE TRANSACTIONS ON GEOSCIENCE AND REMOTE SENSING*, 63, 1-15

Wang, H., Mao, K., Yuan, Z., Shi, J., Cao, M., Qin, Z., Duan, S., & Tang, B. (2021). A method for land surface temperature retrieval based on model-data-knowledge-driven and deep learning. *REMOTE SENSING OF ENVIRONMENT*, 265, 112665

Wang, K., Wan, Z., Wang, P., Sparrow, M., Liu, J., Zhou, X., & Haginoya, S. (2005). Estimation of surface long wave radiation and broadband emissivity using Moderate Resolution Imaging Spectroradiometer (MODIS) land surface temperature/emissivity products. *Journal of Geophysical Research: Atmospheres*, 110

Wang, M., He, G., Zhang, Z., Wang, G., Wang, Z., Yin, R., Cui, S., Wu, Z., & Cao, X. (2019). A radiance-based split-window algorithm for land surface temperature retrieval: Theory and application to MODIS data. *International Journal of Applied Earth Observation and Geoinformation*, 76, 204-217

Wang, M., Zhang, Z., He, G., Wang, G., Long, T., & Peng, Y. (2016). An enhanced single-channel algorithm for retrieving land surface temperature from Landsat series data. *Journal of Geophysical Research*

- Willard, J., Jia, X., Xu, S., Steinbach, M., & Kumar, V. (2022). Integrating Scientific Knowledge with Machine Learning for Engineering and Environmental Systems. *ACM COMPUTING SURVEYS*, 55
- Xie, K., Liang, D., Qin, Y., Wang, Q., & Li, H. (2024). Method for identifying boundary conditions of CFST arches using physically enhanced machine learning. *MECHANICAL SYSTEMS AND SIGNAL PROCESSING*, 213, 111335
- Yu, W., Ma, M., Li, Z., Tan, J., & Wu, A. (2017). New Scheme for Validating Remote-Sensing Land Surface Temperature Products with Station Observations. *Remote Sensing*, 9, 1210
- Yu, W., Ma, M., Wang, X., Geng, L., Tan, J., & Shi, J. (2014). Evaluation of MODIS LST Products Using Longwave Radiation Ground Measurements in the Northern Arid Region of China. *Remote Sensing*, 6, 11494-11517
- Yu, W., Ma, M., Wang, X., Song, Y., & Tan, J. (2011). Validation of MODIS land surface temperature products using ground measurements in the Heihe River Basin, China. *Proceedings of SPIE - The International Society for Optical Engineering*, 8174, 772-783
- Yu, X., Guo, X., & Wu, Z. (2014). Land Surface Temperature Retrieval from Landsat 8 TIRS—Comparison between Radiative Transfer Equation-Based Method, Split Window Algorithm and Single Channel Method. *Remote Sensing*, 6, 9829-9852
- Yuan, Q., Shen, H., Li, T., Li, Z., Li, S., Jiang, Y., Xu, H., Tan, W., Yang, Q., Wang, J., Gao, J., & Zhang, L. (2020). Deep learning in environmental remote sensing: Achievements and challenges. *REMOTE SENSING OF ENVIRONMENT*, 241, 111716
- Zou, M., Zhong, L., Ma, Y., Wang, X., Fu, Y., & Su, Z. (2023). Retrieval of All-Sky Land Surface Temperature Considering Penetration Effect Using Spaceborne Thermal and Microwave Radiometry. *IEEE TRANSACTIONS ON GEOSCIENCE AND REMOTE SENSING*, 61, 1-12